Supplementary Information

Enabling *P*-type Conduction in Bilayer WS_2 with NbP Topological Semimetal Contacts

Lauren Hoang[1,#], Asir Intisar Khan[1,#], Robert K.A. Bennett[1], Hyun-mi Kim[2], Zhepeng Zhang[3], Marisa Hocking[3], Ae Rim Choi[4], Anh Tuan Hoang[3], Il-Kwon Oh[4], Andrew J. Mannix[3,5*], and Eric Pop[1,3,6,7*]

[1]*Department of Electrical Engineering, Stanford University, Stanford, CA 94305, USA*

[2]*Korea Electronics Technology Institute, Seongnam-si 13509, Republic of Korea*

[3]*Department of Materials Science & Engineering, Stanford University, Stanford, CA 94305, USA*

[4]*Department of Intelligence Semiconductor Engineering, Ajou University, Suwon 16499, Republic of Korea*

[5]*Stanford Institute for Materials & Energy Sciences, SLAC National Accelerator Lab., Menlo Park, CA 94025, USA*

[6]*Department of Applied Physics, Stanford University, Stanford, CA 94305, USA*

[7]*Precourt Institute for Energy, Stanford University, Stanford, CA 94305, USA*

[#]*These authors contributed equally to this work.*

[*]*E-mail: ajmannix@stanford.edu, epop@stanford.edu*

This file includes

Supplementary Figures S1-S15
Supplementary Sections I and II
Table S1

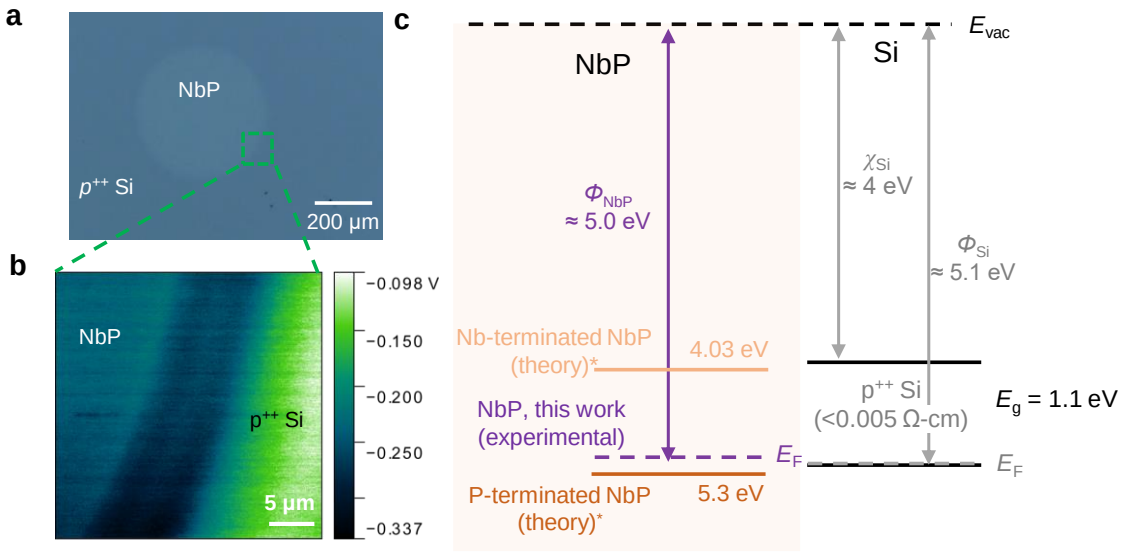

Supplementary Fig. S1 | a, Top-down optical microscope image of NbP semimetal sputter-deposited (~ 4.3 nm thick) on top of a shadow mask on p^{++} Si. Brightness and contrast has been adjusted to enhance visibility of the NbP on Si. **b,** Kelvin probe force microscopy (KPFM) mapping of work function difference ($\Delta\Phi$) between NbP and p^{++} Si substrate ($\Delta\Phi$ = 0.082 eV). The square mapped region corresponds to the green dashed square in panel **a**. Four total scans mapping the work function were taken, with an average $\Delta\Phi$ = 0.080 eV ± 0.028 eV. **c**, Schematic diagram of NbP and p^{++} Si band alignments. Given the work function of p^{++} Si is Φ_{Si} ≈ 5.1 eV, the work function of NbP is estimated to be ~5 eV. The expected work function of NbP (marked by *) is based on calculations from Ref. [1]. The experimentally estimated work function of our NbP films is more similar to the P-terminated NbP theoretical calculations.

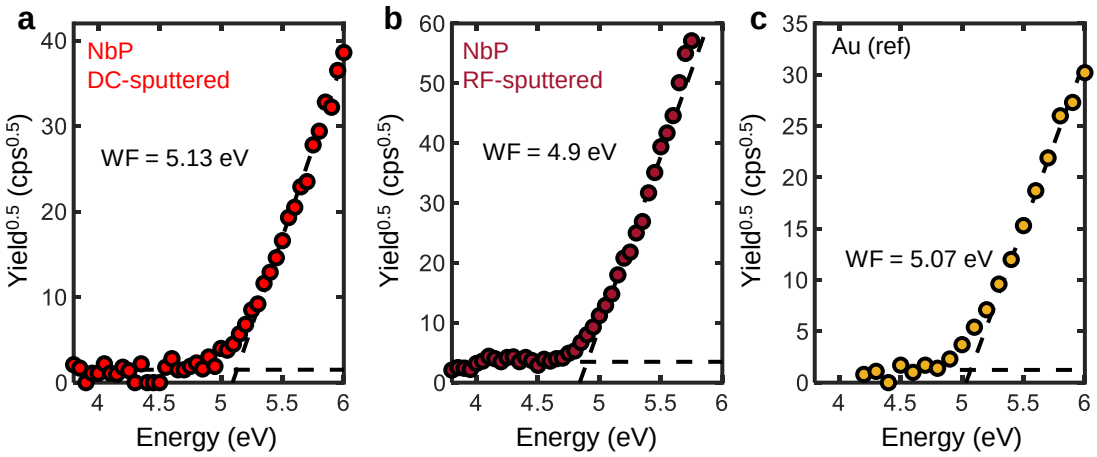

Supplementary Fig. S2 | Photoelectron spectroscopy in air (PESA) measurement. a, PESA spectra of DC-sputtered NbP for 180 s (~3.5 nm), extracting a work function (WF) of 5.13 eV. **b**, PESA spectra for RF-sputtered NbP at 12 W for 20 minutes. A work function of 4.9 eV was found. **c**, PESA spectra for a reference Au sample, with a work function of 5.07 eV.

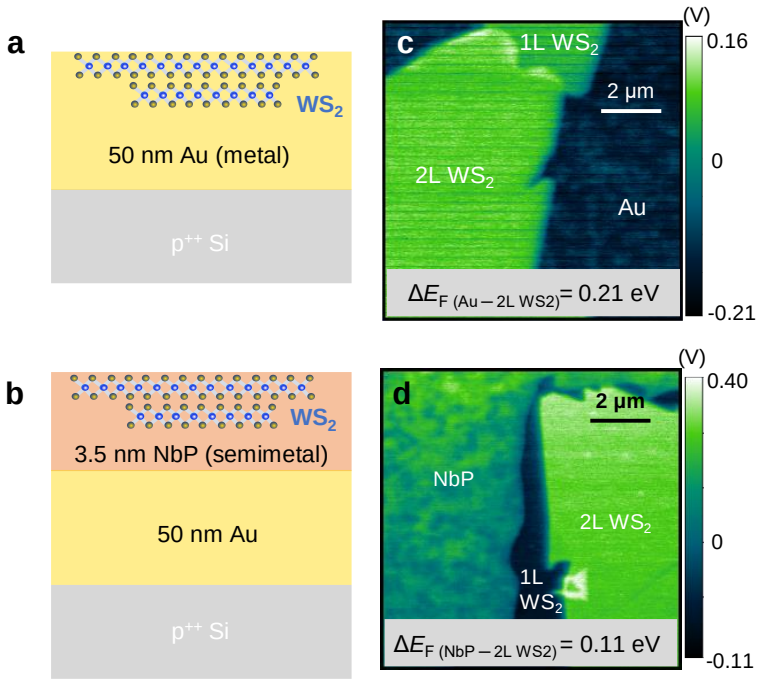

Supplementary Fig. S3 | Kelvin Probe Force Microscopy (KPFM) measurements. Cross-sectional schematics of bilayer WS_2 interface, **a,** with evaporated Au and **b,** with sputtered NbP semimetal (capped by Au). Note that during KPFM characterization the sample was flipped to probe the clean WS_2 surface as in panel **a,b**. Panels **a,b** correspond to material sandwiches used for **c,** KPFM mapping of work function difference between Au/WS_2 and **d,** NbP/WS_2.

We performed Kelvin Probe Force Microscopy (KPFM) measurements to compare NbP/WS_2 and Au/WS_2 interfaces. We sputter-deposited ~3.5 nm NbP directly onto monolayer and bilayer WS_2 regions (grown by chemical vapor deposition, CVD), capped by ~50 nm evaporated Au. For control samples, we evaporated ~50 nm of Au directly onto similar WS_2 regions. After the Au evaporation, a highly doped Si piece was glued to the Au metal film using a thin Epotek H20E epoxy. A tungsten rod was then attached to the back of the CVD-grown WS_2 using the same epoxy. The rod, along with the growth substrate, was subsequently knocked off prior to imaging. This reveals the clean WS_2 surface and mimics the contact material (metal or semimetals) stacks on WS_2 (**Supplementary Fig. S3a,b**). Frequency-modulated Kelvin probe force microscopy (FM-KPFM) was performed in a Bruker Dimension Icon using the PF-KPFM experiment module. An NSC18 Pt probe (nominal spring constant = 2.8 N/m) was used with a lift height of < 25 nm for all measurements. KPFM measurements reveal that the work function difference of bilayer WS_2 with Au is 0.21 eV (**Supplementary Fig. S3c**), but only 0.11 eV with NbP (**Supplementary Fig. S3d**). Thus, we expect our NbP contacts with bilayer WS_2 to have a reduced barrier height, which is favorable for *p*-type conduction. We note that the work function of the monolayer WS_2 regions under NbP deposition shifts from the expected work function of the monolayer WS_2 on Au, probably due to damage experienced from the sputter-deposition of NbP (also see **Supplementary Fig. S4a,d**).

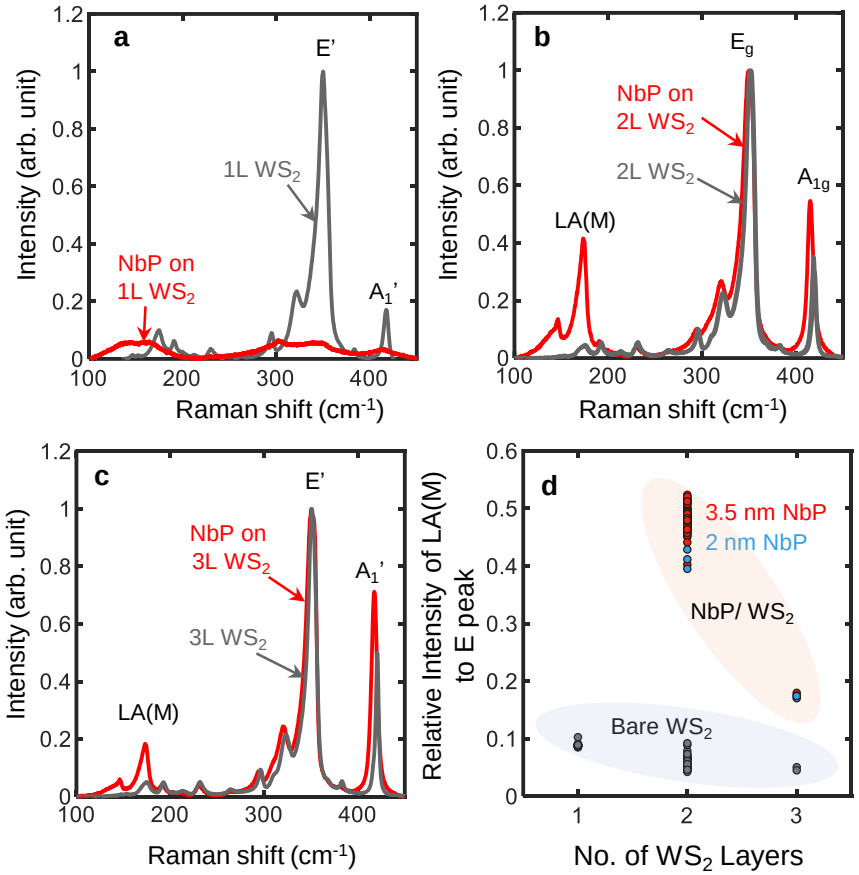

Supplementary Fig. S4 | Raman spectra of WS_2 before (gray) and after (red) NbP deposition for **a,** monolayer (1L) WS_2, **b,** bilayer (2L) WS_2, and **c,** trilayer (3L) WS_2. Raman spectra for monolayer WS_2 before deposition (gray) in **a** and all the spectra in **b** and **c** are normalized to the E peak intensity of the respective WS_2 film (i.e. E' for monolayer and trilayer, E_g for bilayer)[2]. **d,** Relative Intensity of LA(M) Raman peak relative to the respective E peak intensity before (gray) and after (red and blue) NbP deposition for different thicknesses of WS_2. The monolayer peak ratio after NbP deposition is not shown, because its Raman peaks are not well-defined, as seen in panel **a**, likely due to NbP sputtering damage.

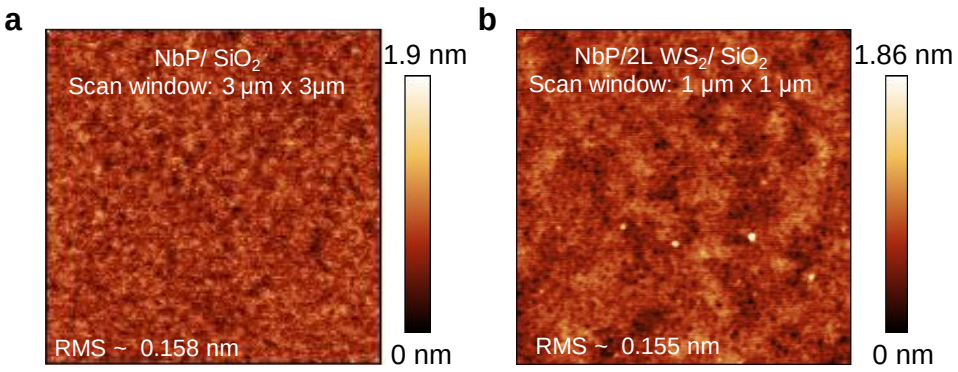

Supplementary Fig. S5 | a, Atomic force microscopy (AFM) image (scan size 3 μm) of ~3.5 nm NbP directly on SiO_2/Si showing low root mean square (RMS) surface roughness of ~0.158 nm. **b,** AFM image (scan size 1 μm) of a ~3.5 nm NbP on bilayer (2L) WS_2 (on SiO_2/Si substrate) showing similar low surface roughness like the case for NbP deposited directly onto SiO_2 (in **a**).

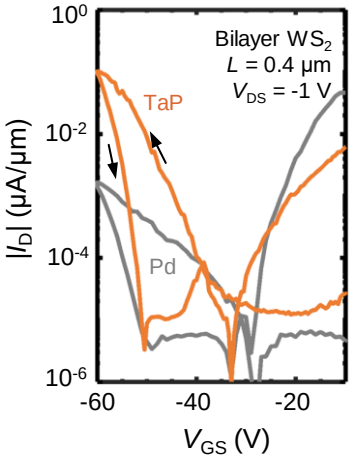

Supplementary Fig. S6 | Drain current (I_D) vs. back-gate voltage (V_{GS}) at V_{DS} = -1 V for bilayer WS_2 transistors with TaP contacts (orange) and Pd contacts (gray), with channel length L_{ch} = 0.4 μm. Small arrows mark forward and backward sweeps, displaying comparable hysteresis for devices with both TaP and Pd contacts.

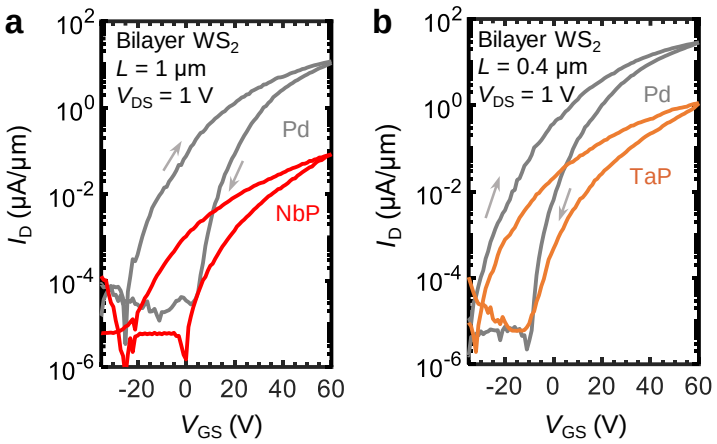

Supplementary Fig. S7 | *n*-type electrical characterization for NbP, TaP, and Pd-contacted bilayer WS_2 Devices. a, Measured drain current (I_D) vs. back-gate voltage (V_{GS}) for bilayer WS_2 transistors (channel lengths L = 1 μm) with NbP contacts (red) and Pd contacts (gray) at V_{DS} = 1 V. Forward and backward sweeps in the measurement display comparable amount of hysteresis for both NbP and Pd contacted devices. **b,** Measured I_D vs. V_{GS} (at V_{DS} = 1 V) for bilayer WS_2 transistors comparing TaP contacts (orange) and Pd contacts (gray) with L = 0.4 μm. In both **a**, and **b**, the electron currents of bilayer WS_2 with our semimetal contacts are significantly suppressed compared to that of the Pd- contacted devices.

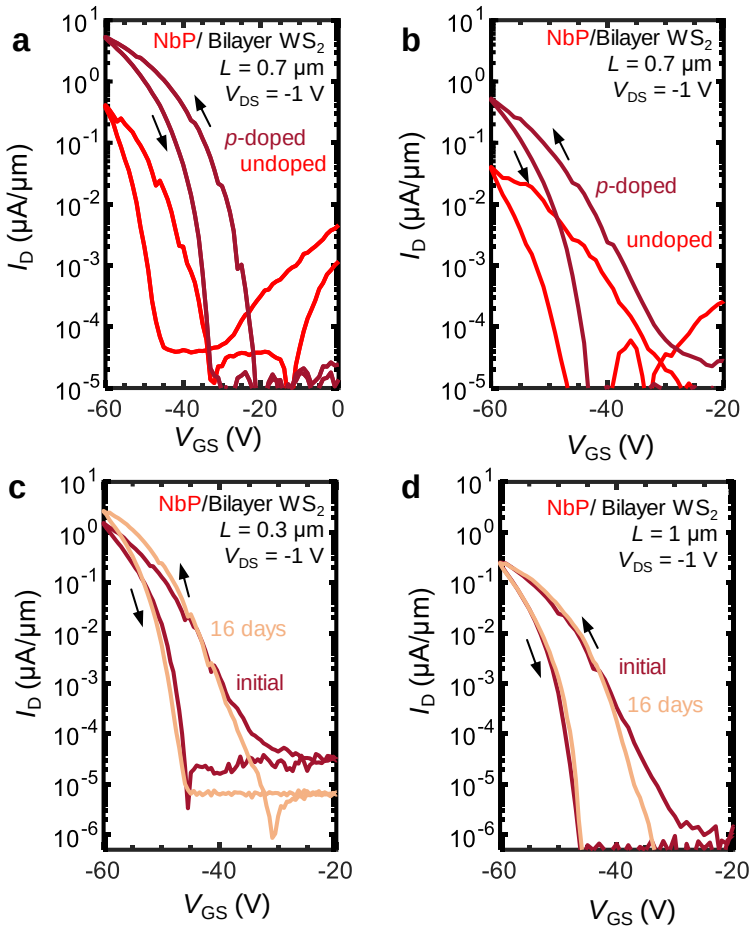

Supplementary Fig. S8 | Additional bilayer WS_2 transistors with NbP semimetal contacts and the impact of additional *p*-type doping. a, Measured I_D vs. V_{GS} for the bilayer WS_2 device shown in **Fig. 3e**, with NbP contacts before (red) and after (dark red) soaking the device in chloroform (*p*-type doping), showing large performance improvement, consistent with **Fig. 3d**. Small arrows mark voltage sweep directions[3]. **b,** Measured I_D vs. V_{GS} for an additional bilayer WS_2 device with NbP contacts before (red) and after (dark red) soaking the device in chloroform (*p*-type doping), showing similar improvement as seen in **Fig. 3d**. **c,** Measured I_D vs. V_{GS} for the bilayer WS_2 device in **Fig. 3d**, showing stable *p*-type behavior after 16 days. **d,** Measured I_D vs. V_{GS} for an additional bilayer WS_2 transistor (chloroform-soaked) with NbP contacts, also showing stable device performance after 16 days. The channel lengths of each device are labeled on the figure panels (e.g., note, L = 0.3 μm in **c** and 1 μm in **d**).

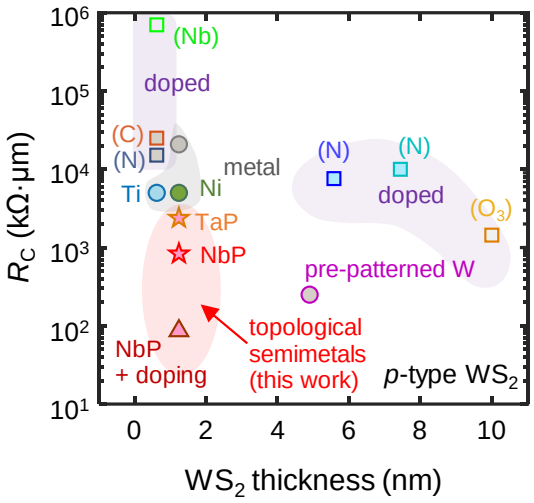

Supplementary Fig. S9 | Benchmarking hole contact resistance (R_C) vs. WS_2 thickness with various contact materials and doping strategies[4–11], including our NbP and TaP semimetals, and control Pd metal. (Text labels in parentheses next to the symbols represent the *p*-type doping type used.) Our results with NbP semimetal contacts and doping enable the lowest *p*-type R_C to date achieved with WS_2 (estimated upper bound of ~80 kΩ·μm), >50× lower than previous reports with sub-2 nm WS_2 thickness. R_C was estimated as half of the total device resistance, which is a good approximation in contact-limited devices and is the upper bound for R_C. This approximation is used because no R_C estimated by the transfer length method (TLM) is available in the literature for *p*-type WS_2.

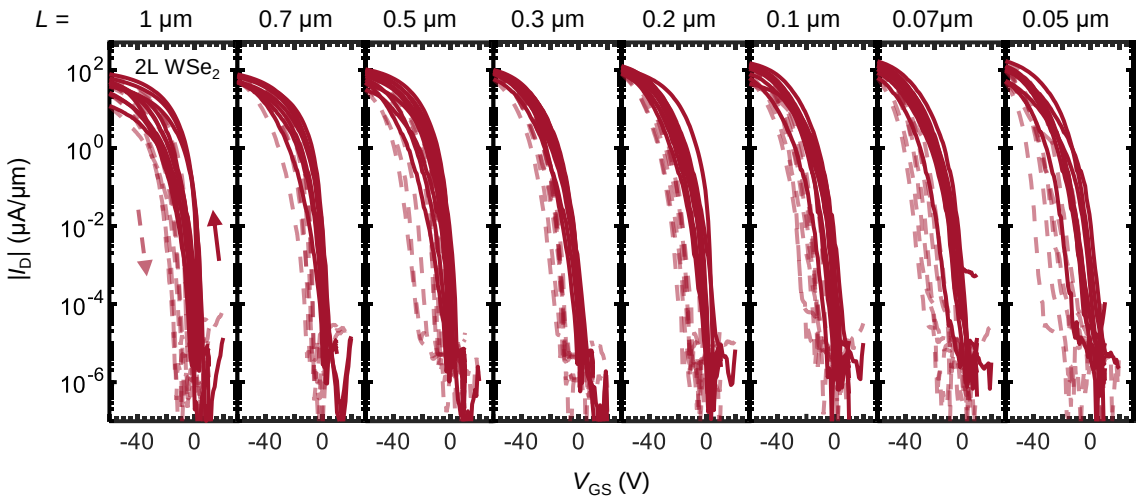

Supplementary Fig. S10 | Measured I_D vs. V_{GS} for *bilayer WSe_2* with NbP-sputtered contacts at various channel lengths (1 μm down to 50 nm). Small arrows mark voltage sweep directions, showing small counter-clockwise hysteresis. Solid lines indicate a sweep from positive to negative V_{GS} and dashed lines represent the negative to positive V_{GS} sweep direction.

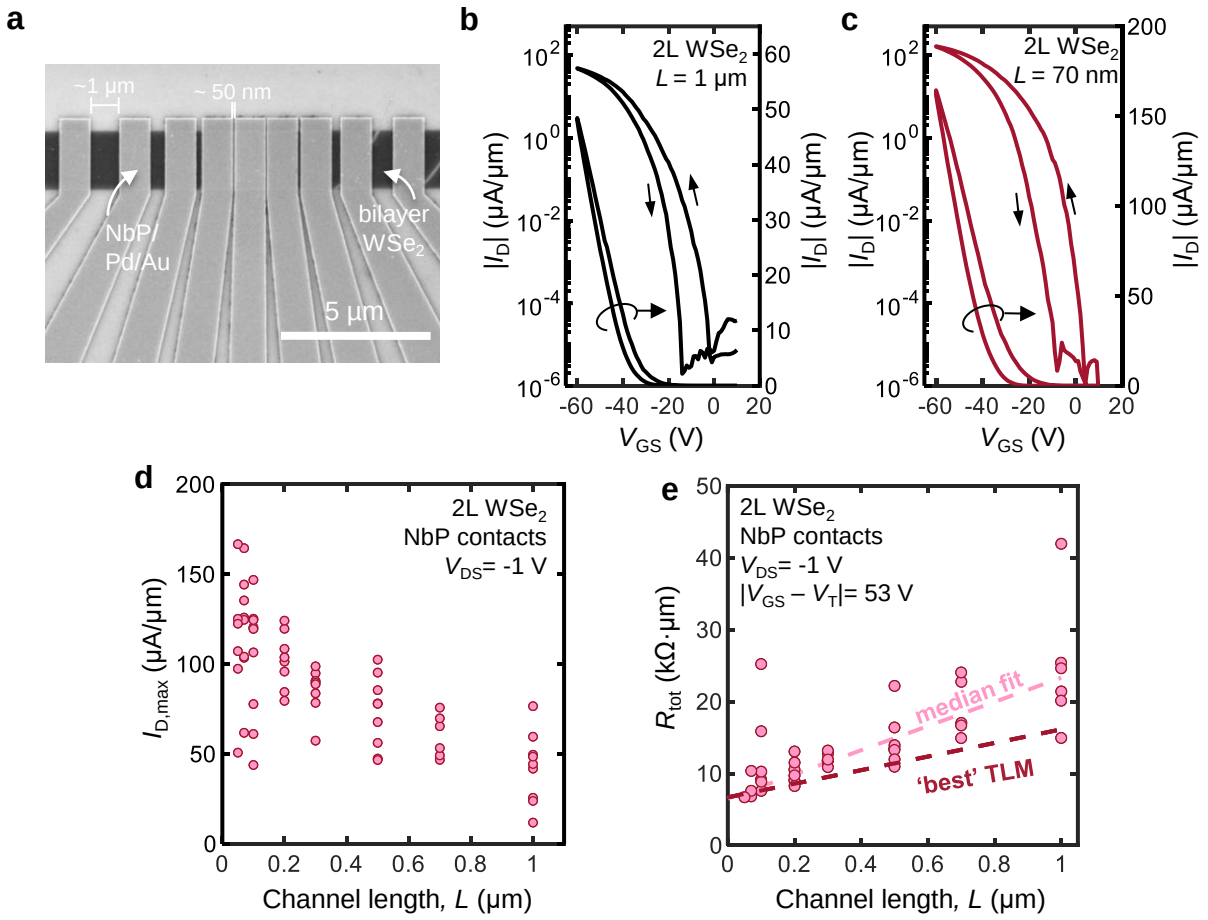

Supplementary Fig. S11 | a, Top-view SEM image of fabricated bilayer WSe_2 devices with NbP contacts capped by Pd/Au. **b,** Measured I_D vs. V_{GS} for the L = 1 μm bilayer WSe_2 device shown in **Fig. 4a**, with NbP contacts, Small arrows mark voltage sweep directions[3]. **c,** Measured I_D vs. V_{GS} for the L = 70 nm bilayer WSe_2 device shown in **Fig. 4a**. **d,** Maximum *p*-type current $|I_{D,max}|$ vs. channel length, L achieved at V_{DS} = -1 V of bilayer WSe_2. A total of 63 devices were measured and shown here. **e**, Total device resistance R_{TOT} vs. channel length, L at V_{DS} = -1 V and overdrive voltage $|V_{GS} – V_T|$ of 53 V, where V_T is extracted at I_{cc} =10 nA/μm. A linear fit of best and median pseudo-TLM is also shown in dashed lines. For R_C extraction (**Fig. 4b**), linear fitting of the devices is repeated for V_{ov} = 10 V to 56 V.

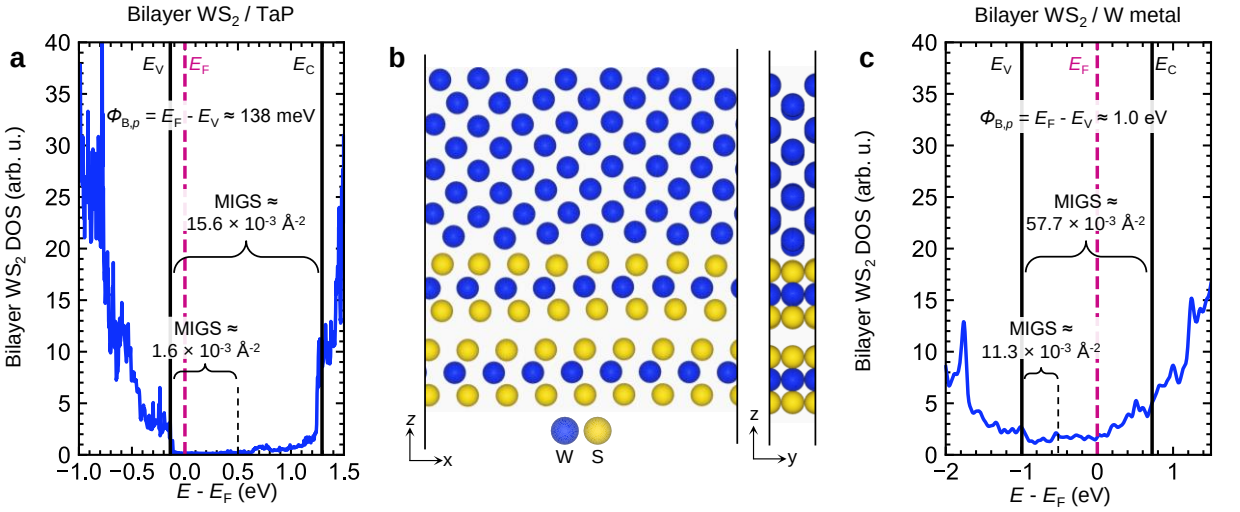

Supplementary Fig. S12 | Density functional theory (DFT) simulations of <u>bilayer</u> WS_2 interfaced with TaP semimetal or W metal. a, Projected density of states (pDOS) contributions from bilayer WS_2 to the overall DOS for a TaP interface with bilayer WS_2. Metal-induced gap states (MIGS) are estimated by integrating the pDOS over the regions as labeled. **b,** Cross-section schematics of the DFT supercell for tungsten (W) with bilayer WS_2. (Left) *x*-*z* cut and (right) *y*-*z* cut. **c,** Projected DOS (pDOS) contributions to the overall DOS for a W interface with bilayer WS_2, showing large *p*-type Schottky barrier $\Phi_{B,p} \approx 1.0$ eV due to E_F pinning from MIGS. The Fermi energy E_F is referenced to zero and marked with a dashed purple line, whereas the valence band maximum E_V and conduction band minimum E_C are marked with solid black lines. Locations of band extrema are determined from projected band structures (see Supplementary Section II). We note that although our simulation suggests a comparable MIGS density and barrier height for TaP/bilayer WS_2 (panel **a**) compared to that of NbP/bilayer WS_2 (**Fig. 4b** in the main text), experimentally our sputter-deposited TaP semimetals do not provide contacts as good as NbP to bilayer WS_2 (**Fig. 3g,h** in the main text), likely due to greater damage during deposition from heavier Ta vs. lighter Nb atoms.

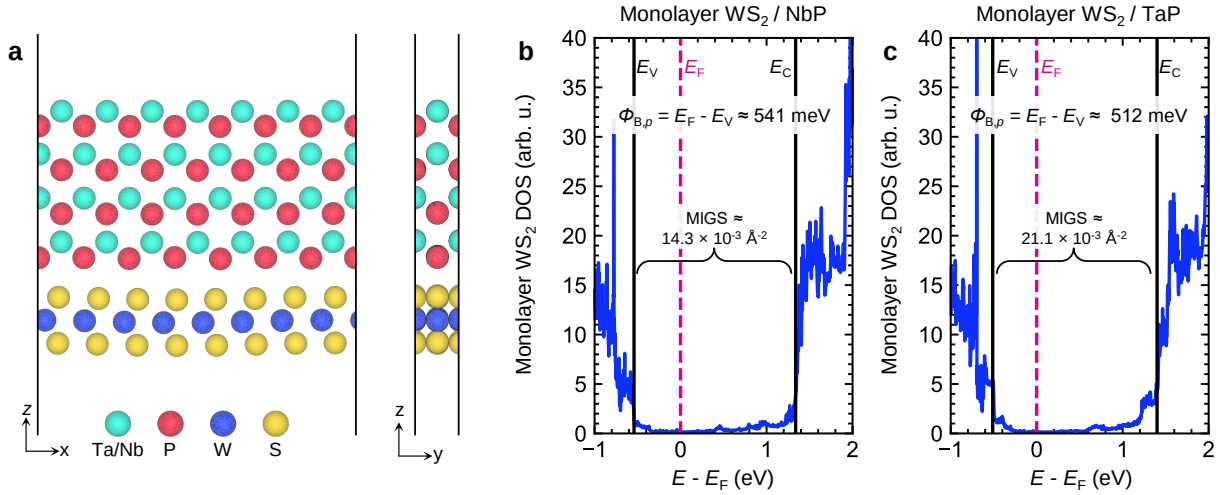

Supplementary Fig. S13 | Density functional theory (DFT) simulations of monolayer WS_2 interfaced with semimetals NbP and TaP. a, Cross-section schematics of the DFT supercell for semimetal (NbP, TaP) with monolayer WS_2. (Left) *x-z* cut and (right) *y-z* cut. Before extracting the density of states (DOS), we initially relaxed the supercell with identical settings as in **Fig. 4.b,** Projected DOS (pDOS) contributions from monolayer WS_2 to the overall DOS for the NbP/monolayer WS_2 interface and **c,** for the TaP/monolayer WS_2 interface, showing that the Fermi energy E_F is pinned inside the band gap. E_F is referenced to zero and marked with a dashed purple line, whereas the valence band maximum E_V and conduction band minimum E_C are marked with solid black lines. Locations of band extrema are determined from projected band structures (see Supplementary Section II). We note the non-negligible $\Phi_{B,p} \approx 0.54$ and 0.51 eV between *monolayer* WS_2 with NbP or TaP, respectively, compared to $\Phi_{B,p} \approx 0.21$ or 0.14 eV for the interface of *bilayer* WS_2 with the same respective semimetals (**Fig. 4b** and **Fig. S12a**).

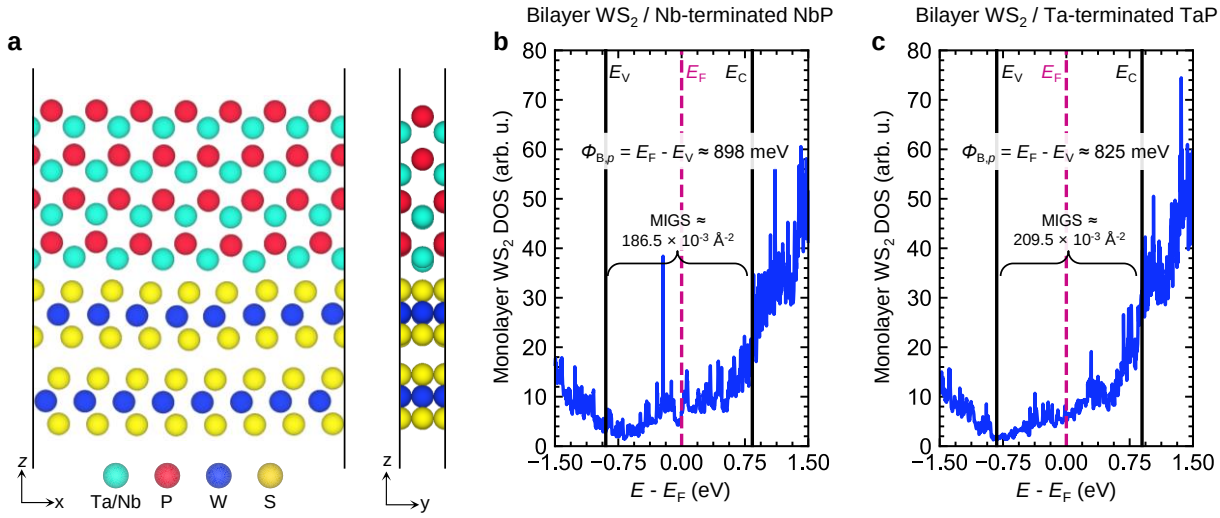

Supplementary Fig. S14 | Density functional theory (DFT) simulations of bilayer WS_2 interfaced with metal-terminated NbP and TaP semimetals. a, Cross-section schematics of the DFT supercell for semimetal (NbP, TaP) with bilayer WS_2. (Left) *x-z* cut and (right) *y-z* cut with Nb or Ta-terminations. **b,** Projected DOS (pDOS) contributions from bilayer WS_2 to the overall DOS for the Nb-terminated NbP/bilayer WS_2 interface and **c,** for the Ta-terminated TaP/bilayer WS_2 interface, showing that the Fermi energy E_F is inside the band gap. The Fermi energy E_F is referenced to zero and marked with a dashed purple line. Locations of band extrema are determined from projected band structures (see Supplementary Section II).

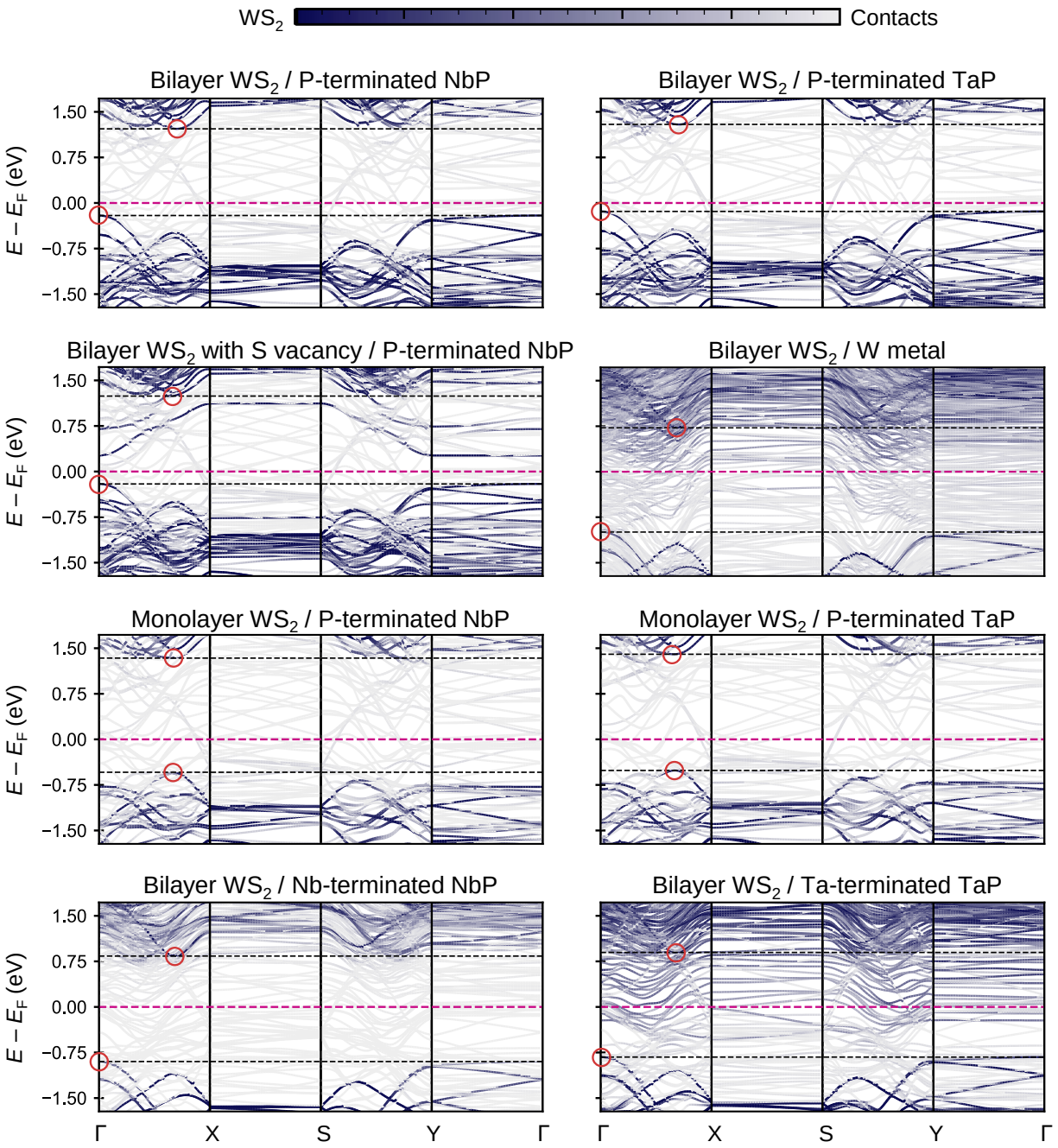

Supplementary Fig. S15 | Density functional theory (DFT) computed projected band structures of the WS_2/contact interfaces discussed throughout the Supplementary Information. Dark blue bands are contributed primarily by WS_2, whereas light gray bands are contributed primarily by the contacts. The title of each plot specifies the number of WS_2 layers (monolayer or bilayer), and the contact used (P- or metal-terminated NbP or TaP, or W). In each plot, the Fermi energy E_F is referenced to 0 and marked with a purple dashed line. The valence and conduction band edges are marked with black horizontal lines. The specific locations of the valence or conduction band edges are highlighted with small red circles.

Supplementary Section I: Density Functional Theory (DFT) Results and Band Alignments

We used DFT to analyze NbP/bilayer WS_2 (main text **Fig. 5a,b**) and TaP/bilayer WS_2 (**Supplementary Fig. S11a**) interfaces using P-terminated configurations. Following the Schottky-Mott rule, the *p*-type Schottky barrier without Fermi pinning is $\Phi_{B,p} = \chi + E_G - \Phi_M$. Here, E_G is the band gap, χ is the electron affinity of the semiconductor, and Φ_M is the work function of the contact material. Using previously calculated values for E_G and χ from DFT estimates[1,12] and taking Φ_M of P-terminated TaP and NbP as 5.4 and 5.3 eV, respectively, we estimate the expected $\Phi_{B,p}$ = -210 meV and -110 meV for bilayer WS_2 interfaces with TaP and NbP, respectively. These values are close to those estimated from DFT simulations in the main text (≈138 meV and 206 meV for TaP/bilayer WS_2 and NbP/bilayer WS_2, respectively), further suggesting that metal-induced gap states (MIGS) do not strongly pin the Fermi energy of our semimetal/bilayer WS_2 heterostructures.

We note that TaP and NbP semimetals could exist in Ta- or Nb-terminated configurations (**Supplementary Fig. S1c**). These terminations have work functions ~1 eV lower than their P-terminated counterparts[1], suggesting that Ta- and Nb- terminations should lead to large hole Schottky barriers when interfaced with bilayer WS_2 purely based on band alignment (i.e., before considering the effect of Fermi energy pinning due to gap states). To confirm this reasoning, we perform additional DFT simulations to extract the density of states (DOS) and hole Schottky barrier heights of bilayer WS_2 with NbP and TaP in their Nb- and Ta-terminated configurations (**Supplementary Fig. S14a**). Indeed, we find that these configurations exhibit large $\Phi_{B,p} \approx 0.90$ and 0.82 eV, respectively (**Supplementary Fig. S14b,c**), as expected based on band alignment.

We also used W as a control metal in our DFT simulations (**Supplementary Fig. S12b,c**) because its lattice constant (3.16 Å) closely matches that of bilayer WS_2 (~3.18 Å). Consequently, we were able to build our W/bilayer WS_2 supercell without having to either (i) significantly strain the W or the bilayer WS_2 (which could spuriously change the MIGS density and/or barrier height) and/or (ii) include a large number of atoms in the supercell to minimize strain (which can drastically increase the computational cost). We anticipate that the result and discussion would remain qualitatively similar if we were to instead use another conventional metal, e.g., Au or Pt[13].

Previous DFT estimates suggest that band gap of <u>monolayer</u> WS_2 is ~0.32 eV greater than that of bilayer WS_2, whereas the two materials have very similar electron affinities[12]. Thus, using the same equation as above, we expect TaP and NbP interfaces with <u>monolayer</u> WS_2 to exhibit hole Schottky barriers of $\Phi_{B,p} \approx 110$ meV and 210 meV, respectively, notably larger than the ideal values above, with <u>bilayer</u> WS_2. (We note that the experimental difference in band gaps between bilayer and monolayer

WS_2 is larger at ~0.46 eV, with ~ 0.33 eV arising from differences in valence band maxima[14].) To validate these calculations, we perform additional DFT simulations using the NbP/monolayer WS_2 and TaP/monolayer WS_2 supercells shown in **Supplementary Fig. S13a**. The extracted density of states (DOS) plotted in **Supplementary Fig. S13b,c** reveal the DFT-computed $\Phi_{B,p} \approx 0.54$ eV and 0.51 eV for NbP and TaP with monolayer WS_2, respectively. This result confirms that the less favorable band alignment of monolayer WS_2 (compared to that of bilayer WS_2) with these semimetals leads to positive hole Schottky barriers at NbP and TaP interfaces with monolayer WS_2.

Supplementary Section II: Density Functional Theory (DFT) Projected Band Structures

Throughout the main text and Supplementary Information, we use the energy of the valence band maxima E_V relative to the Fermi energy E_F to calculate the *p*-type Schottky barrier height as $\Phi_{B,p} = E_F - E_V$. We also calculate the MIGS density by integrating the WS_2 projected density of states (pDOS) between E_V and the conduction band minimum E_C. To better estimate E_V and E_C for these calculations, we extracted the projected band structures using PyProcar[15] for each WS_2/contact interface studied in this work and manually found the energies that correspond to these band extrema (**Supplementary Fig. S15**). For all band structure calculations, we used the relaxed structures from the original pDOS calculations and performed self-consistent calculations as described in the main text, this time using electron occupations described by Gaussian smearing (spreading coefficient of 0.0025 Ry). Afterwards, we extracted the band structures using at least 45 *k*-points between each high symmetry point along the $\Gamma \rightarrow X \rightarrow S \rightarrow Y \rightarrow \Gamma$ path.

Table S1: Extracted Parameters for Different Contact/WS_2 Interfaces from Density Function Theory

WS_2	**Contact material**	**$\Phi_{B,p}$ (meV)**	**MIGS (× 10^{-3} $Å^{-2}$)**
2L WS_2	NbP (P-terminated)	206	10.7 (across full band gap) 1.5 (within 0.5 eV of valence band)
2L WS_2 with S vacancies (~1.4 × 10^{14} cm^{-2})	NbP (P-terminated)	204	52.8 (across full band gap)
2L WS_2	TaP (P-terminated)	138	15,6 (across full band gap) 1.6 (within 0.5 eV of valence band)
2L WS_2	Tungsten	996	57.7 (across full band gap) 11.3 (within 0.5 eV of valence band)
2L WS_2	NbP (Nb-terminated)	898	186.5 (across full band gap)
2L WS_2	TaP (Ta-terminated)	825	209.5 (across full band gap)
1L WS_2	NbP (P-terminated)	541	14.3 (across full band gap)
1L WS_2	TaP (P-terminated)	512	21.1 (across full band gap)

Supplementary References:

1. Yang, N. *et al.* Ab Initio Computational Screening and Performance Assessment of van der Waals and Semimetallic Contacts to Monolayer WSe_2 P-Type Field-Effect Transistors. *IEEE Trans. Electron Devices* **70**, 2090–2097 (2023).
2. Scheuschner, N., Gillen, R., Staiger, M. & Maultzsch, J. Interlayer resonant Raman modes in few-layer MoS_2. *Phys. Rev. B - Condens. Matter Mater. Phys.* **91**, (2015).
3. Cheng, Z. *et al.* How to report and benchmark emerging field-effect transistors. *Nat. Electron.* **5**, 416–423 (2022).
4. Tang, B. *et al.* Direct n- to p-Type Channel Conversion in Monolayer/Few-Layer WS_2 Field-Effect Transistors by Atomic Nitrogen Treatment. *ACS Nano* **12**, 2506–2513 (2018).
5. Zhang, F. *et al.* Carbon doping of WS_2 monolayers: Bandgap reduction and p-type doping transport. *Sci. Adv.* **5**, 5003–5027 (2019).
6. Asselberghs, I. *et al.* Wafer-scale integration of double gated WS_2-transistors in 300mm Si CMOS fab. in *2020 IEEE International Electron Devices Meeting (IEDM)* 40.2.1-40.2.4 (IEEE, 2020). doi:10.1109/IEDM13553.2020.9371926.
7. Lin, D. *et al.* Dual gate synthetic WS_2 MOSFETs with 120μS/μm Gm 2.7μF/cm^2 capacitance and ambipolar channel. in *2020 IEEE International Electron Devices Meeting (IEDM)* 3.6.1-3.6.4 (IEEE, 2020). doi:10.1109/IEDM13553.2020.9372055.
8. Zhang, P. *et al.* Transition-Metal Substitution-Induced Lattice Strain and Electrical Polarity Reversal in Monolayer WS_2. *ACS Appl. Mater. Interfaces* **12**, 18650–18659 (2020).
9. Chung, Y.-Y. *et al.* Demonstration of 40-nm Channel Length Top-Gate p-MOSFET of WS_2 Channel Directly Grown on SiO_x/Si Substrates Using Area-Selective CVD Technology. *IEEE Trans. Electron Devices* **66**, 5381–5386 (2019).
10. Cao, Q. *et al.* Realizing Stable p-Type Transporting in Two-Dimensional WS_2 Films. *ACS Appl. Mater. Interfaces* **9**, 18215–18221 (2017).
11. Kato, R. *et al.* p-Type Conversion of WS_2 and WSe_2 by Position-Selective Oxidation Doping and Its Application in Top Gate Transistors. *ACS Appl. Mater. Interfaces* **15**, 26977–26984 (2023).
12. Kim, H. & Choi, H. J. Thickness dependence of work function, ionization energy, and electron affinity of Mo and W dichalcogenides from DFT and GW calculations. *Phys. Rev. B* **103**, 85404 (2021).
13. Tang, H. *et al.* Schottky Contact in Monolayer WS_2 Field-Effect Transistors. *Adv. Theory Simulations* **2**, 1900001 (2019).
14. Li, D., Wang, X., Mo, X., Tse, E. C. M. & Cui, X. Electronic gap characterization at mesoscopic scale via scanning probe microscopy under ambient conditions. *Nat. Commun.* **13**, 4648 (2022).
15. Herath, U., Tavadze, P. & He, X. PyProcar: A Python library for electronic structure pre/post-processing. *Comput. Phys. Commun.* **251**, 107080 (2020).